High-speed photogrammetry system for measuring the kinematics of insect wings

Iain D. Wallace, Nicholas J. Lawson, Andrew R. Harvey, Julian D. C. Jones, and Andrew J. Moore

We describe and characterize an experimental system to perform shape measurements on deformable objects using high-speed close-range photogrammetry. The eventual application is to extract the kinematics of several marked points on an insect wing during tethered and hovering flight. We investigate the performance of the system with a small number of views and determine an empirical relation between the mean pixel error of the optimization routine and the position error. Velocity and acceleration are calculated by numerical differencing, and their relation to the position errors is verified. For a field of view of ~40 mm × 40 mm, a rms accuracy of 30 μm in position, 150 mm/s in velocity, and 750 m/s^2 in acceleration at 5000 frames/s is achieved. This accuracy is sufficient to measure the kinematics of hoverfly flight. © 2006 Optical Society of America

OCIS codes: 120.0120, 120.6650.

1. Introduction

The subject of photogrammetry, in which the shape of an object is measured from photographic or electronic images, is one with a long tradition. Long-range photogrammetry was used to survey buildings from high vantage points in the 1850s and developed into aerial photogrammetry in the early 20th century. Close-range photogrammetry, in which the camera is not focused at infinity, has been used extensively in machine vision, surveying buildings and ancient artifacts, plastic surgery, analysis of traffic accidents, and many other fields.[1] Our particular interest is to measure the kinematics (position, velocity, and acceleration) for a grid of points on the surface of the wings of tethered and free-hovering hoverflies. The wings are typically 13 mm in length and beat at 150 Hz, giving a maximum wing-tip velocity of approximately 10 m/s. These data are to be used in an aeroelastic model of flapping flight that treats the wing as a deformable topographic surface (i.e., interacting, elastic elements), which in turn will be used in the design of man-made micro air vehicles.

Experimental data for insect wing deformation at a dense grid of points during free flight are difficult to obtain, and, to the best of our knowledge, no reports have been found in the literature. Single-point laser triangulation has been reported for insect wings attached to a translation stage,[2] but, to the best of our knowledge, no measurements have been made from tethered or free-flying insects. High-speed imaging has been used to measure the wing angle with respect to the body plane (flapping angle) and the wing tilt with respect to the stroke plane (torsional angle), assuming that the wing behaves as a rigid plate.[3,4] An analysis of the wing as a half-rigid plate has been reported[5] in which the wing is divided into a number of chordwise strips that can rotate independently about the longitudinal axis of the wing. The torsional angles of each strip were estimated by matching the static, digitized wing outline to the varying outline from high-speed camera measurement. However, the half-rigid model is not applicable to insects whose chord deformation (camber) is significant, such as hoverflies and dragonflies. Wing camber measurements on tethered[6] and free-flying[7] dragonflies were made using a stripe projection technique. Approximately seven stripes were projected into a calibrated measurement volume, and the camber between the stripe centers was estimated by interpolation. The stripe-projection method was also applied to a moth tethered to a force balance for a simultaneous

I. D. Wallace, A. R. Harvey, J. D. C. Jones, and A. J. Moore (a.moore@hw.ac.uk) are with the School of Engineering and Physical Sciences, Heriot–Watt University, Edinburgh, EH14 4AS, United Kingdom. N. J. Lawson is with the Department of Aerospace Sciences, Cranfield University, Cranfield, MK43 0AL, United Kingdom.

Received 31 August 2005; revised 28 November 2005; accepted 28 November 2005; posted 1 December 2005 (Doc. ID 64563).

0003-6935/06/174165-09$15.00/0

estimate of the aerodynamic force generated by the wings.[8] Data could not be gathered for the whole wing beat due to the large variation in wing orientation with respect to the projected fringes. Moth wings are opaque, whereas dragonfly wings contain a dense structure of interconnected spars that enabled the projected stripes to be identified. The spar structure in hoverflies is too sparse for projected fringes to be visible.

Photogrammetry at such small spatiotemporal scales has only recently become practical due to the availability of high-speed digital cameras of accessible cost. Our application requirements fall between those of traditional photogrammetry applications. Human motion analysis uses relatively low-speed cameras (e.g., 25 Hz) that provide high spatial resolution to identify unique markers on the subject. Vehicle crash testing requires high-speed cameras to verify that crumple zones have activated in the correct sequence and the manual identification of a small number of targets (often <10) to verify that human-occupancy zones have been preserved at discrete instants through the sequence.

In this paper we characterize the performance of a high-speed photogrammetry system that we have devised for measuring the kinematics of insect wings during tethered and free flight. We use pulsed laser illumination at a wavelength that is invisible to the insects of interest. White-light illumination cannot be used with hoverflies because continuous illumination of sufficient brightness that enables the microsecond camera exposure required to effectively freeze motion causes the insects to overheat, and visible pulsed illumination interrupts the insects' natural wingbeat frequency. In this paper we quantify the effect of laser speckle in both static and dynamic measurements. The insect wings change shape between successive images, and so the number of views is restricted to the number of high-speed cameras available. We characterize the system performance at a small number of views and determine the errors in the velocity and acceleration calculated from the position data. Finally, we consider the effect of irregular spots on the magnitudes of errors for shape measurement on a static housefly wing.

2. Methodology

Our implementation of photogrammetry consists of three stages: (i) calibration of lens distortions and the camera's internal parameters and an initial estimate of the camera's external parameters; (ii) intersection, to give an initial estimate of the positions of the unknown points on the object; and (iii) bundle adjustment, in which errors in the estimates of the camera's parameters and the positions of the object points are reduced through optimization. These three stages are described in Subsections 2.A–2.C.

A. Lens Calibration and Initial Estimate of Camera's External Parameters

A central perspective projection model, Fig. 1, is frequently used in photogrammetry to represent the

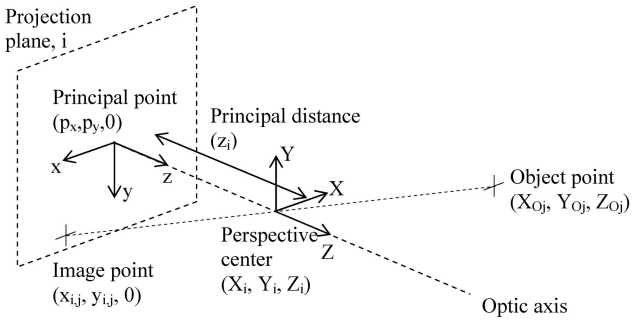

Fig. 1. Central perspective of projection model for camera i, viewing point j.

mapping of a point in 3D object space into a point on the 2D image plane of a camera. A projective transformation is the most general mapping in which straight lines are preserved. Hence the model can find the 3D structure (for the noise-free case) only to within some systematic error introduced by the projective transformation of the real structure. Camera calibration from a known target is required to accommodate the differences between the real camera and lens and the ideal pinhole camera modeled.

The projection of $j = 1, \ldots, n$ 3D structure points $\mathbf{X_{Oj}} = (X_{Oj}; Y_{Oj}; Z_{Oj}; 1)$ in homogeneous coordinates to 2D image points in normalized pixel units (assuming a constant principal distance of z_i in image i) $\mathbf{x_{i,j}} = (x_{i,j}/z_i, y_{i,j}/z_i, 1)$ viewed in $i = 1, \ldots, m$ cameras can be expressed[9] as

$$\mathbf{x_{i,j}} = M_i \mathbf{X_{Oj}}, \quad i = 1, \ldots, m, \; j = 1, \ldots, n, \quad (1)$$

where $x_{i,j}$ and $y_{i,j}$ are defined relative to an origin at the principal point, (p_x, p_y), the intersection of the optic axis with the image plane. Multiplying out Eq. (1) yields the collinearity equations for each point, which state that an object point, the perspective center, and its image point are collinear:

$$x_{i,j} = z_i \frac{m_{i,11}X_{Oj} + m_{i,12}Y_{Oj} + m_{i,13}Z_{Oj} + m_{i,14}}{m_{i,31}XO_j + m_{i,32}Y_{Oj} + m_{i,33}Z_{Oj} + m_{i,34}},$$

$$y_{i,j} = z_i \frac{m_{i,21}X_{Oj} + m_{i,22}Y_{Oj} + m_{i,23}Z_{Oj} + m_{i,24}}{m_{i,31}X_{Oj} + m_{i,32}Y_{Oj} + m_{i,33}Z_{Oj} + m_{i,34}}. \quad (2)$$

$m_{i,11}$ to $m_{i,34}$ represent the elements of the 3×4 mapping matrix, M_i, of camera i. M_i may be decomposed as $M_i = K_i(R_i \mid -R_i t_i)$, where t_i represents the position of the perspective center and R_i is the rotation matrix of camera i. Quaternions are used to represent the rotation as these are inherently more stable than Euler angles and are not prone to gimbal lock.[10] The 3×3 matrix K_i represents the camera's internal calibration parameters that convert the coordinate vector of the image point to normalized pixel units[9]:

$$K_i = \begin{bmatrix} f_x & sf_x & p_x \\ 0 & f_y & p_y \\ 0 & 0 & 1 \end{bmatrix}, \quad (3)$$

where f_x and f_y are the magnifications in units of pixels/mm in the x- and y-coordinate directions, respectively, and s accommodates any skewing of the coordinate axes. For a CCD camera with square pixel cameras and orthogonal axes of the sensor array, $s = 0, f_x = f_y = f$.

The ideal-central-perspective projection model is extended to incorporate systematic radial and decentering camera lens distortions.[11] Radial lens distortion produces a displacement of the imaged point $(\Delta x_r, \Delta y_r)$, which depends on the radial distance $r^2 = (x^2 + y^2)^{1/2}$ from the principal point, given by

$$\Delta x_r = (x/r)(k_1 r^3 + k_2 r^5 + k_3 r^7 + \ldots),$$

$$\Delta y_r = (y/r)(k_1 r^3 + k_2 r^5 + k_3 r^7 + \ldots), \quad (4)$$

where $k_1, k_2, \ldots$ are the coefficients of radial distortion. Decentering distortion, due to the noncollinearity of optical elements of the lens, introduces a radial and tangential displacement of the imaged point $(\Delta x_d, \Delta y_d)$, given by

$$\Delta x_d = p_2(r^2 + 2x^2) + 2p_1 xy,$$

$$\Delta y_d = p_1(r^2 + 2y^2) + 2p_2 xy, \quad (5)$$

where p_1 and p_2 are the coefficients of tangential distortion. Equations (4) and (5) are incorporated into Eq. (1) to obtain the corrected model in terms of $x + \Delta x_r + \Delta x_d$ and $y + \Delta y_r + \Delta y_d$.

To calibrate the cameras, several images are taken of a known calibration object at various positions and angles to the camera. The solution to the collinearity equations, Eqs. (2), is found with a gradient descent method (or alternatively an iterative least-squares estimator) to calculate the camera's internal parameters (principal distance, principal point, and lens distortion parameters) and an initial estimate of the camera's external parameters (camera position and orientation).

B. Intersection

Following the system's calibration, images of the test object are recorded. By using the camera's internal parameters and the initial estimate of the camera's external parameters as calculated in Subsection 2.A, the collinearity equations are used to provide a least-squares estimate of the position of points on the test object. This process is known as intersection,[1] and it provides an initial estimate for the bundle adjustment.

C. Bundle Adjustment

Bundle adjustment[12] is a general technique that minimizes the error between measured values and a predictive parametric model. A bundle adjustment is used to optimize the projective camera model and the derived 3D structure to best fit the point measurements in all camera images. The collinearity equations, Eqs. (2), provide a functional relation between the image coordinates $x_{i,j}$ and the mapping matrix and the structure points:

$$\mathbf{x_{i,j}} = f_i(\mathbf{C_i}, \mathbf{M_i}, \mathbf{X_{Oj}}), \quad (6)$$

where $\mathbf{C_i}$ contains camera calibration factors including the principal distance and the lens distortion parameters. We seek to modify the vectors in the functional relation such that the residual between the measured image coordinates $\hat{\mathbf{x}}_{\mathbf{i,j}}$ and predicted image coordinates $\mathbf{x_{i,j}}$, $\mathbf{L} = \hat{\mathbf{x}}_{\mathbf{i,j}} - \mathbf{x_{i,j}}$, is minimized in a least-squares sense. The initial estimate of the predicted image coordinates, $\mathbf{x_{i,j}}$, provided by intersection (Subsection 2.B) is improved iteratively by adding an adjustment $\boldsymbol{\delta}$ to the vectors in the functional relation, assuming that the functional relation is locally linear. The iterative adjustments are determined from the Gauss–Newton or normal equations

$$J^T J\delta = -J^T \mathbf{L}, \quad (7)$$

where J is the Jacobian matrix, the matrix of partial differentials of $\mathbf{x_{i,j}}$ with respect to each vector in the functional relation. In our implementation, a Newton iteration [Eq. (7)] or a Levenberg–Marquardt[13] iteration is used to solve the equations until the sum of the squared adjustments falls below a tolerance value. The mean pixel error (MPE) is then given by

$$\mathrm{MPE} = \frac{1}{mn} \sum_{i=1}^{m} \sum_{j=1}^{n} L^2. \quad (8)$$

Depending on the implementation, we may allow only the motion ($\mathbf{M_i}$); motion and structure ($\mathbf{M_i}$ and $\mathbf{X_{Oj}}$); or motion, structure, and calibration factors ($\mathbf{M_i}$, $\mathbf{X_{Oj}}$, and $\mathbf{C_i}$) to be optimized. For example, for the case where only the motion parameters are to be optimized, $J = \partial \mathbf{x_{i,j}}/\partial M_i$. For the results presented here, the bundle adjustment includes $\mathbf{M_i}$, $\mathbf{X_{Oj}}$, and $\mathbf{C_i}$, where $\mathbf{C_i}$ is restricted to the principal distance only.

3. Experimental System

The experimental setup is shown schematically in Fig. 2 for the case of a laser illumination with up to four cameras. A diode laser bar produced an elliptical beam at 808 nm with a maximum output power of 200 W, a maximum pulse duration of 80 μs, and a maximum repetition rate of 5000 Hz. The coherence length of the laser diode bar was not determined because it comprised several independent emitters. The laser beam was focused by a 75 mm focal length lens onto a fiber array of four 2 m lengths of high-NA (0.39), large-core (1 mm) plastic optical fiber. The input fiber ends were stripped of buffer to 10 mm, sandwiched adjacent to each other between microscope

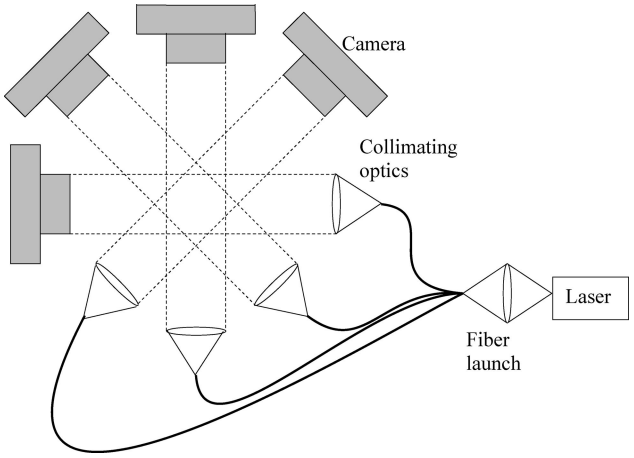

Fig. 2. Schematic of experimental setup with laser illumination.

slides, and fixed with epoxy. The fiber end faces were then polished plane for launching light into the fiber and to remove any excess epoxy. The output fiber ends were stripped of buffer to 60 mm and mounted individually in fiber-optic chucks. The output light from each fiber was expanded through a 50.8 mm focal length lens to produce 60 mm diameter collimated beams that shone through the measurement volume toward the camera. The fiber illuminators can be repositioned to enable imaging of scattered light from nontransparent objects such as moth wings. Speckle noise was evident in the laser-illuminated images.

White-light illumination was used with calibration targets and static insect wings to act as a baseline for the measurements made with laser illumination. Transparent targets were again viewed in transmission by illuminating a white card placed behind the target with the light from 15 W, 12 V halogen lamps.

For the experiments reported here, two synchronized high-speed digital cameras were used at half-frame resolution (1280 $\times$ 512 pixels) with 105 mm focal length macro lenses (designed for use with 35 mm cameras). The camera-to-subject distance was approximately 400 mm. The laser pulses were synchronized as slave to a transistor-transistor logic (TTL) signal taken from the camera pair. Static and dynamic calibration experiments were performed on two multifrequency grid distortion targets. The calibration target for static measurements comprised a glass substrate with chrome spots spaced at 2, 1, and 0.5 mm with a spot center-to-center spacing accuracy specified at ± 2.5 μm. The target used for dynamic measurements comprised a white Mylar substrate with printed spots spaced at 6, 3, and 1.5 mm with a spot center-to-center spacing specified at ± 13 μm. The correspondences between spots in different views of the targets were determined manually.

4. Results

Initially we performed static photogrammetry to establish a baseline for the system's performance. The first measurements were made on the best quality target available to us: the glass calibration target. Further static measurements were made on a section of the Mylar target attached to a stationary optical chopper, with both white-light and laser illumination. Dynamic photogrammetry was performed on the Mylar target using the optical chopper to introduce a controlled rigid body motion at a speed representative of the insect wing motion. Finally, measurements from a static insect wing were made.

A. Static Close-Range Photogrammetry

A single camera was used to record 48 images of a region of the glass distortion target containing 6 $\times$ 26 chrome spots (1 mm spacing) held at various arbitrary positions and orientations within the measurement volume with white-light illumination. The spots were approximately 20 pixels in diameter in the image. Although the grid was regular, no regularity was assumed for the processing and the analysis was equivalent to that of arbitrarily placed spots on an arbitrary object. A correlation method was used to locate the centers of the spots in the image.

The (X, Y, Z) positions of all 156 points in the measurement region were calculated using the procedure outline in Section 2. The error between the measured and nominal spot positions over all the measured points was calculated, taking the nominal target position such that the mean error was zero. The standard deviation of the error is plotted against the number of camera views in Fig. 3(a). For numbers of views less than the total number of views available (48), the mean of the standard deviation calculated from all possible combinations of views is plotted. A decrease in error with the number of views is seen. The X and Y errors at large numbers of views become comparable to the uncertainty of ± 2.5 μm in dot-to-dot spacing of the calibration target. The out-of-plane error (Z) dominates at all numbers of views. An independent measurement of the Z-spot positions was made with a white-light interferometer with a resolution of 20 nm. The result for 26 target spots in each of the six rows is shown in Fig. 4, and confirms that the Z error is not due to a nonplanar target. Figure 4 also includes the photogrammetry results for the 156 target spots for one of the combinations of four views. In general, the lowest ratio of Z to (X, Y) errors is obtained when the included angle between camera views is 90° and the cameras are positioned symmetrically about the target.[14]

Figure 3(b) shows the mean MPE, again calculated from all possible combinations of views from the 48 images used to generate Fig. 3(a). The error bars represent one standard deviation in the MPE. The mean MPE plateaus at 0.10 pixels with a standard deviation of 0.04. The MPE is reduced for fewer views because the camera model is less constrained for fewer image points. We have determined that the empirical curve $0.10 \times (1 - 1/N)$ fits the data quite well [Fig. 3(b)], where N is the number of views. It is instructive to compare the standard deviation of the error between the measured and nominal spot posi-

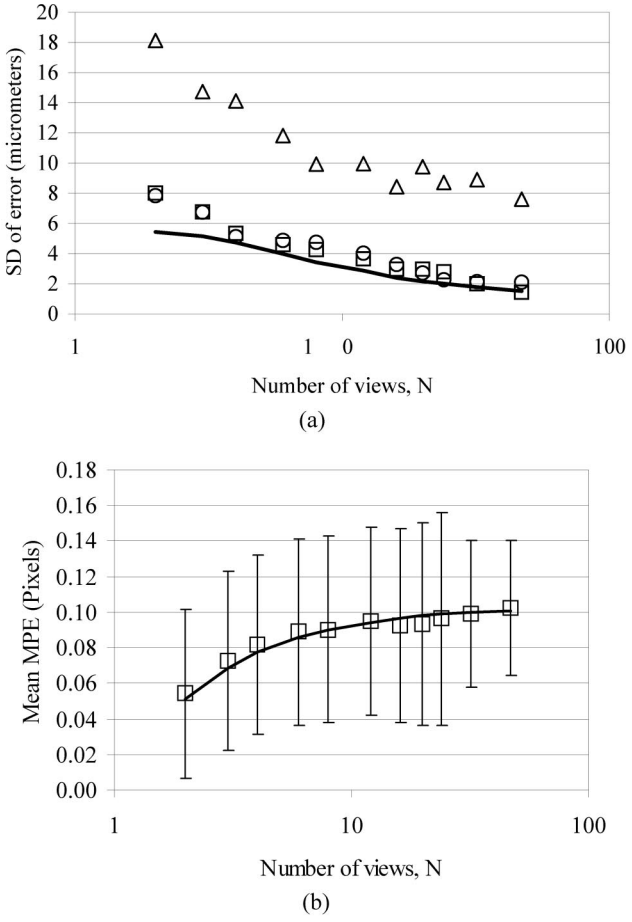

Fig. 3. (a) Standard deviation of error for X (circles), Y (squares), and Z (triangles) directions. The solid curve shows empirical error based on MPE and the number of views. (b) MPE (squares) with ± 1 standard deviation (SD) error bars. The solid curve shows an empirical curve $0.1 \times (1-1/N)$.

tions [Fig. 3(a)], with the expected error calculated from the MPE. The longest side of the glass calibration target is 50 mm, corresponding to 498 pixels when the side was aligned with the horizontal image axis. The error is expected to be MPE $\times$ 50/(498 $\times$ $\sqrt{(N-1)}$), assuming that error is proportional to $1/\sqrt{(N-1)}$, which simplifies to 5 $\times$ $\sqrt{(N-1)}/(498 \times N)$ μm. This curve is plotted as a solid line in Fig. 3(a) and gives a good approximation to the X and Y error.

Further static measurements were made from the Mylar distortion target containing 6 $\times$ 6 spots (with 6 mm spacing) attached to the optical chopper. The chopper was manually rotated to various positions, and static images were recorded under laser and white-light illumination. The images were acquired at 974.50 $\pm$ 0.02 frames/s, half-frame (1280 $\times$ 512) with a $f/1.4$ aperture. Exposures of 10 μs (white light) and 5 μs (laser) were used. The standard deviation of the error between the measured and the nominal spot positions was calculated as described above. The results are summarized in Table 1. The

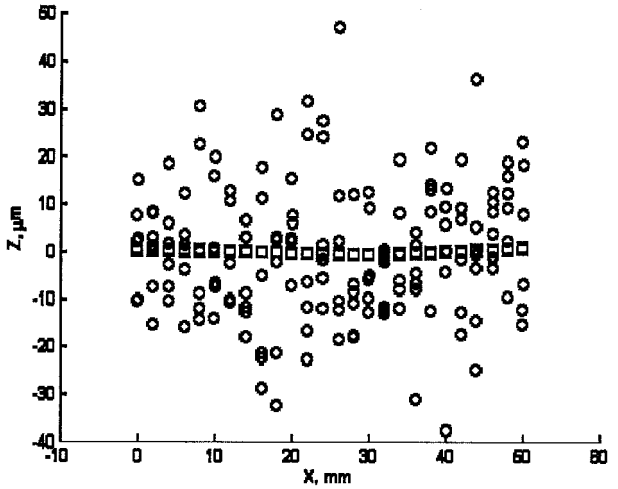

Fig. 4. Calibration target spot Z height measured with white-light interferometer (squares), looking edge on to 26 $\times$ 6 measurement points. Static photogrammetry measurement (circles) calculated from four views.

results for two views are the mean of five stereo image pairs (ten views total) for white light and six pairs (12 views total) for laser illumination. The total number of views for each illumination can be combined for this rigid object, and the results are also shown in the second set of columns in Table 1. The error for white-light illumination for all views is comparable to the ± 13 μm uncertainty in the spot spacing for the Mylar target. The errors are larger under laser illumination than those observed for white light, and they are attributed to the laser speckle's reducing the accuracy with which spot centroids can be located.

B. Dynamic Close-Range Photogrammetry

For dynamic photogrammetry measurements, the chopper was rotated at 593 $\pm$ 9 rpm. The size of the grid and the rotation speed were chosen as representative of a locust wing (with a wing length of 50 mm and a maximum wing-tip speed of 5 m/s). The range of spot speeds from direct calculation was 4.3–5.7 m/s corresponding to a radius of rotation, r, of 69.1 mm $\leq r \leq$ 91.6 mm. The velocity of the grid was independently measured by a laser vibrometer (Polytec, OFV-5000). The laser spot from the vibrometer was visible in the stereo images to allow comparison with the velocities measured by photogrammetry. The spot speed from photogrammetry for a position close to the vibrometer spot was found to be 5.03 $\pm$ 0.12 m/s and from the vibrometer 5.06 $\pm$ 0.07 m/s. In addition, a direct calculation from the rotation frequency and radius of the vibrometer spot yielded 5.02 $\pm$ 0.12 m/s.

Seven image pairs were recorded in white-light and laser illumination. The standard deviation of the error between the measured and nominal spot positions was calculated as described above, and the results for the dynamic target are shown in Table 1. The most important observation is that the errors for the laser illumination between the static and the dynamic

Table 1. Standard Deviation of Errors in Position (*X*, *Y*, *Z*) Relative to the Nominal Calibration Target Position for a Mylar Target Mounted to an Optical Chopper

Illumination	Number of Views	MPE	Error (μm): Two Views				Error (μm): All Views			
			X	*Y*	*Z*	Total	*X*	*Y*	*Z*	Total
Static close range photogrammetry										
White light	10	0.06	11	13	19	25	3	10	14	17
Laser	12	0.10	22	26	29	45	12	14	13	23
Dynamic close range photogrammetry										
White light	14	0.19	12	16	39	44	5	8	29	31
Laser	14	0.14	22	21	26	39	5	11	17	21

cases are similar. The distribution of the errors under the laser illumination that was used to calculate the standard deviation in Table 1 is plotted in Fig. 5 and is normally distributed indicating that random errors dominate over systematic errors. Under white-light illumination, the errors for dynamic photogrammetry are greater (approximately double) than those for the static measurement. The reduced performance is attributed to the effect of motion blur. The spots moved approximately 50 μm (1/60 of their diameter or 0.5 pixels) during the 10 μs camera exposure.

Our interest is in deriving the kinematics, and eventually the dynamics, of insect wings in flight, and therefore requires a knowledge of the errors associated with numerical differentiation of the photogrammetry position data. Therefore velocities and accelerations of points on the chopper were calculated for laser illumination. Initially, the velocities and accelerations of points on the chopper were determined from the displacements of each point during the interval, *t*, between consecutive frames.

The calculated velocity at each point was converted to angular velocity, ω. The radius of rotation of each point was calculated by fitting a circle to the 3D trajectory using a least-squares Gauss–Newton solver. Figure 6(a) shows the difference between the angu-

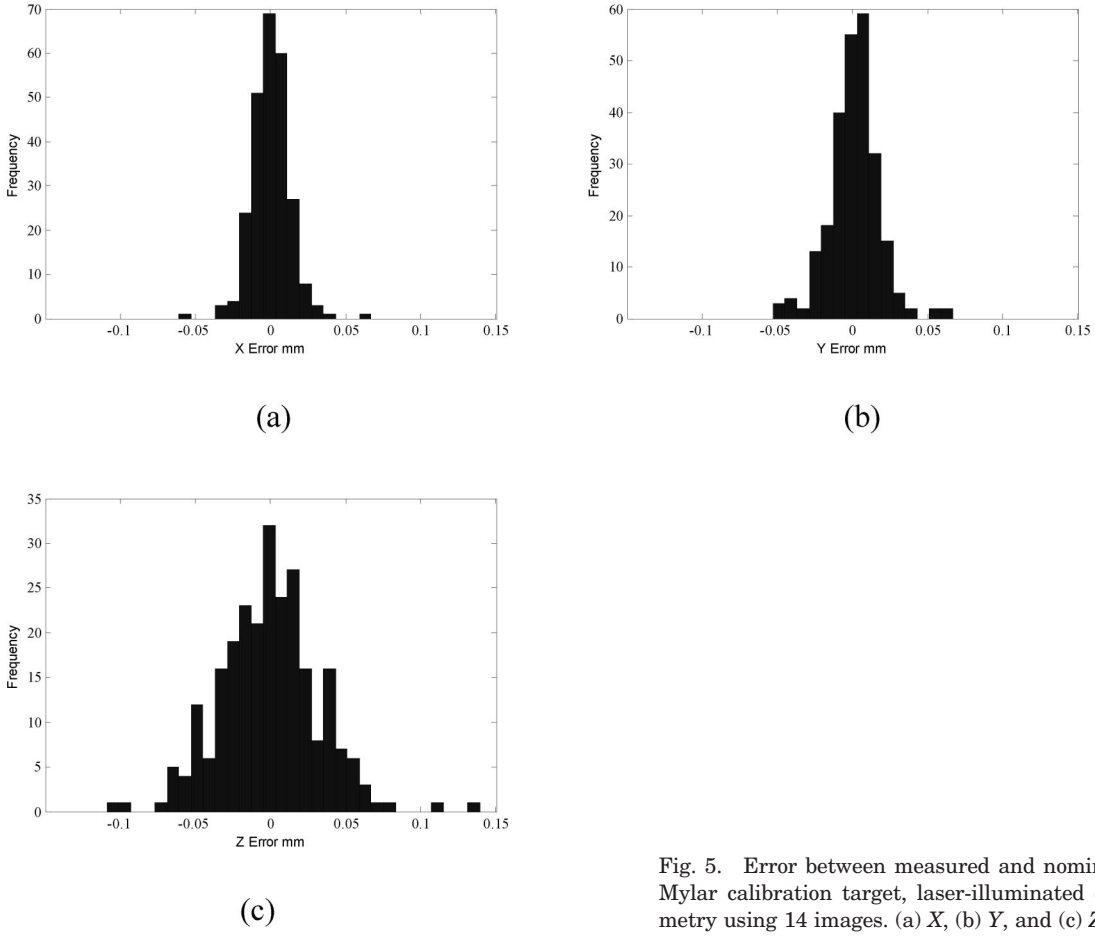

Fig. 5. Error between measured and nominal spot positions on Mylar calibration target, laser-illuminated dynamic photogrammetry using 14 images. (a) *X*, (b) *Y*, and (c) *Z* directions.

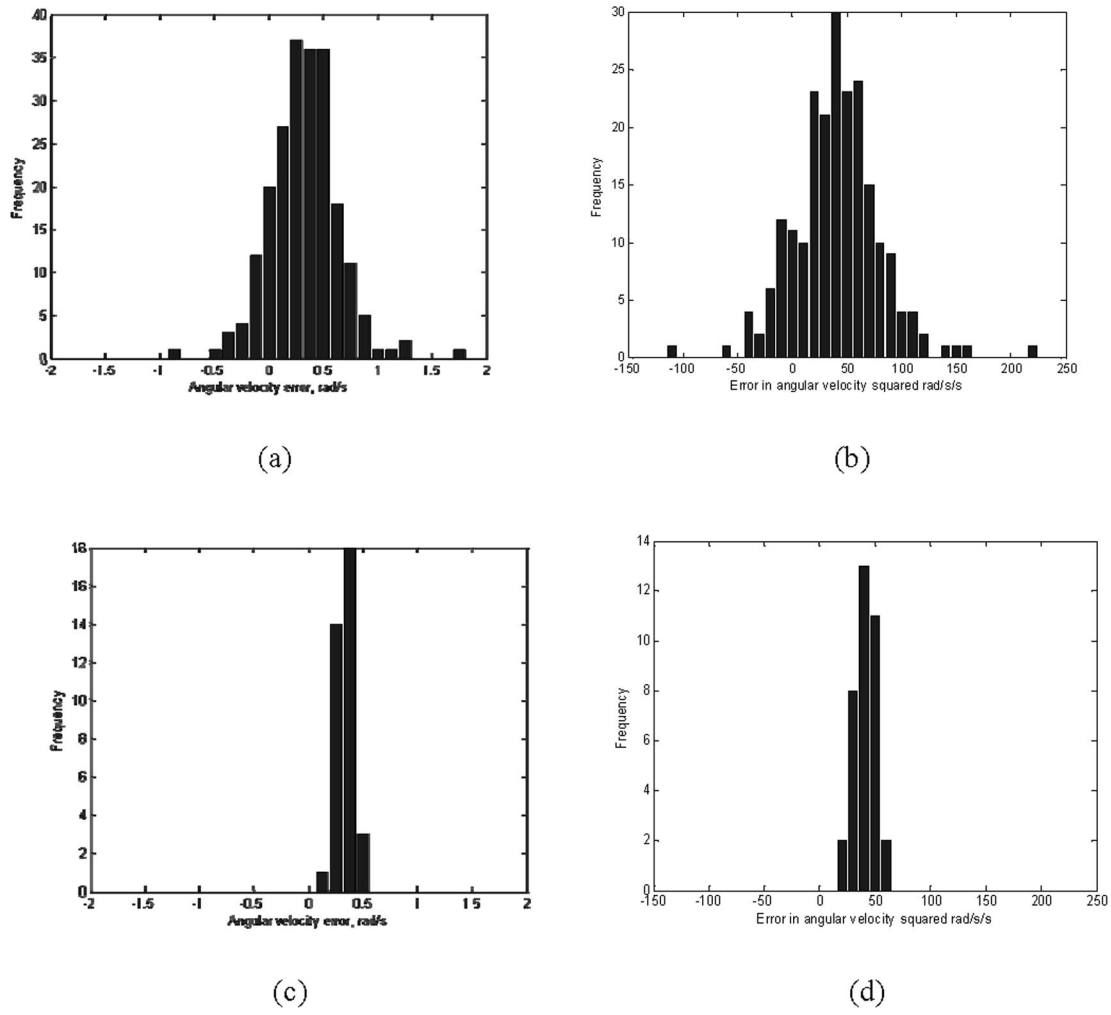

Fig. 6. Error in (a) angular velocity and (b) normalized acceleration (angular velocity squared) relative to the nominal angular velocity of the Mylar calibration target, laser-illuminated dynamic photogrammetry using 14 images. Error in (c) angular velocity and (d) normalized acceleration relative to the nominal angular velocity after least-squares circle fit to spot trajectories.

lar velocity measured by photogrammetry (a mean 62.5 ± 0.3 rad/s or 597 ± 3 rpm) and the nominal value taken from the optical chopper controller (62.2 rad/s or 593 rpm) for all 216 measured velocity values (i.e., six positions of the 6 × 6 grid of points). The mean of the distribution is offset by 0.3 rad/s, which is within the accuracy of the nominal angular velocity measurement. The standard deviation of the angular velocity, σ_ω, can be related to the standard deviation in the position measurements (σ_d = 21 μm from Table 1) using the relation $\sigma_\omega = \sigma_d/(tr)$ assuming that t and r have negligible error. For the range of radii of rotation used here, a range of $0.22 \leq \sigma_\omega \leq 0.30$ rad/s is predicted.

Figure 6(b) shows the difference between the centripetal acceleration, a_c, measured by photogrammetry (mean 5 ± 39 m/s^2) and the nominal value taken from the optical chopper controller, normalized by the radius of rotation at each point, for all 180 measured acceleration values (i.e., five positions of the 6 × 6 grid of points). The mean of the normalized acceleration distribution is offset and is related to the offset in angular velocity by the relation $\delta a_c = 2\omega\delta\omega = 37.3$ (rad/s)^2. The standard deviation of the normalized centripetal acceleration, σ_{ac}, can be related to the standard deviation in the position measurements using the relation $\sigma_{ac} = 2\sigma_d/t^2 = 39.9$ (rad/s)^2.

Several techniques can be used to reduce errors in the velocity and acceleration measurements compared to the simple numerical difference applied above. One procedure applicable to insect flight is to determine an equation (e.g., polynomial) describing the position against time that best fits the experimental data, which can then be differentiated analytically. For the constant angular velocity around the center of rotation of the points on the optical chopper, a fit to the points around a circular path and a fixed center of rotation was already performed. Figure 6(c) shows the difference between the angular velocity measured from the fitted photogrammetry data and the nominal value taken from the optical chopper

Fig. 7. Example image of a housefly wing taken under laser illumination.

controller for 36 measured velocity values (i.e., the angular velocity for each of the 6×6 grid of points). The standard deviation has been reduced to $0.3/\sqrt{7} = 0.11$ rad/s. Similarly, Fig. 6(d) shows the difference between the fitted centripetal acceleration measured by photogrammetry and the nominal value taken from the optical chopper controller, normalized by the radius of rotation at each point, for 36 measured acceleration values (i.e., the normalized centripetal acceleration for each of the 6×6 grid of points). The standard deviation has been reduced to $39.9/\sqrt{7} = 7.9$ (rad/s)^2.

C. Static Wing Measurements

In a final experiment to demonstrate the feasibility of recording insect-wing kinematics, a housefly (*Musca domestica*) wing was marked with 78 spots using an indelible ink marker pen with a sharpened tip. The wing was mounted on the blade of the optical chopper, rotated to various positions, and static images were recorded under laser illumination in transmission. We chose to make static rather than dynamic measurements because we wished to avoid the risk that air resistance on the wing would introduce unknown vibration and flutter; however, we know from tests on the calibration targets that the accuracy of measurement in the static and dynamic cases when using laser illumination is comparable. An example image taken under laser illumination is given in Fig. 7. Images of the glass calibration target in transmission were also recorded for direct comparison. Table 2 shows the standard deviation of errors. In this case, errors with the housefly wing target are quoted relative to the mean of the measurements because the wing shape and spot position were not known *a priori.* As before, the errors for the glass calibration target were calculated relative to the nominal spot positions and are similar to those achieved in Fig. 3. However, the housefly results show greater errors compared to those for the calibration target. The reduced accuracy is due to the irregularity of the drawn wing spots and the resulting degradation achieved on the MPE. To demonstrate this effect, one image was taken from the data set of the housefly wing viewed approximately normal, and positions of the spot centers were calculated by using the correlation software. The image was then stretched to simulate a change in its viewing angle to approximately 45° to perpendicular, and the recovered spots' centers differed by 0.7 ± 0.4 pixels in comparison with the original data. When a similar exercise was performed for views of the circular spots on the glass calibration target, the calculated centers between the two views differed by 0.08 ± 0.05 pixels. Repeating the exercise with artificially generated circles and ellipses produced similar results to those for the calibration target—circles yielded 0.09 ± 0.05 pixels and ellipses yielded 0.2 ± 0.1 and 0.12 ± 0.09 pixels along the major and minor axes, respectively. Therefore in both the hand-drawn and calibration-target spot examples, the difference in the positions of recovered spot centers due to image tilt is similar to that for the experimentally determined MPE.

Table 2. Standard Deviation of Errors in Position (*X*, *Y*, *Z*) Relative to the Mean Position for a Housefly Wing and Relative to the Nominal Position for a Glass Calibration Target

Illumination	Number of Views	MPE	Error (μm): All Views			
			X	*Y*	*Z*	Total
Wing	10	0.80	13	15	18	26
Target	10	0.15	1.3	1.7	2.9	3.6

5. Discussion

We have described an experimental system that will be used to implement high-speed close-range photogrammetry on tethered and free-flying insects. White-light illumination was found to provide lower MPE and position errors than did laser illumination for static targets, due to the laser speckle's downgrading of image quality. Although the performance of white-light and laser illumination becomes similar for a large number of views, the cost of high-speed cameras currently restricts the number of views. Thus for many targets, white-light illumination would be preferred. However, for the current application, laser illumination was chosen so as to avoid any heating effects and to be invisible to the insects under test and therefore not influence their natural wing-flapping behavior. It was demonstrated that the errors in static and dynamic measurements were comparable for laser illumination.

In the dynamic calibration experiments, the effective number of camera views in the case of a rigid target was increased by combining successive images in a time sequence taken with a small number of cameras. Clearly this is not the case with dynamic measurements of deformable objects such as insect wings, in which the number of views is restricted to the number of cameras available. The measurement error decreases, and the MPE increases, as the number of views increases. An empirical relation between

the MPE and position error was found. This relationship can be used to estimate the expected magnitude of the error for each point depending on the number of views of a given point at a given time instant, taking into account that points are frequently obscured due to wing motion.

It was demonstrated that errors in position can be used to predict the range of errors in velocity and acceleration. Estimating a value of 30 μm for the total positional error to be expected from an insect flight experiment, the velocity error at 5000 frames/s is then 150 mm/s and the acceleration error is 750 m/s^2. The expected maximum velocities and accelerations for the hoverfly are 10 m/s, and 5000 m/s^2, respectively, and therefore the system provides data from a grid of points with sufficient accuracy for entomological studies based on topological surfaces rather than strips. We are also undertaking some preliminary experiments on tethered locusts, which fly reliably under laboratory conditions. Locust wings are four times larger than those of houseflies, and the expected total error will scale with the field of view to 120 μm. Our locust experiments are typically conducted at 1000 frames/s, and the expected velocity and acceleration errors are then 120 mm/s and 120 m/s^2, respectively. The expected maximum velocities and accelerations for a locust are 5 m/s and 250 m/s^2, respectively, and some additional fitting will be required to reduce errors adequately. Dynamic measurements will benefit from smaller, more circular marked spots to reduce the MPE. We are investigating improving measurement accuracy by improving the circularity of the markings, although eventually we wish to measure wings with no additional markings by using instead the natural vein structure of the wing.

6. Conclusions

This paper describes an experimental characterization of a dynamic close-range photogrammetry system targeted at deformable objects, specifically, the wings of a hoverfly in tethered and free flight. In the photogrammetry of dynamic deformable objects, the number of views of the object is restricted to the number of cameras, unlike that for rigid bodies or static photogrammetry where images from a temporal sequence can be combined to improve accuracy. Position error was shown to decrease and the MPE was shown to increase with an increasing number of views. Dynamic and static photogrammetry measurements were reported for an object under both laser and white-light illumination. For the laser, the dynamic results were similar to those obtained for a static object. Point velocities and accelerations were determined by numerical differentiation, and errors were in agreement with those predicted from shape measurement. Point velocities derived from photogrammetry showed good agreement with laser vibrometer measurement. A simple model of the motion was used to reduce errors. The results indicate that high-speed dynamic measurements of the deformation of insect wings during flight will be possible with the new system.

The authors acknowledge the UK Engineering and Physical Science Research Council (EPSRC) and UK Defence Science and Technology Laboratory (DSTL) for jointly funding this research under grant GR/S23032. A. J. Moore acknowledges the EPSRC for the provision of funding via the Advanced Fellowship Programme. The authors acknowledge the U.S. Defense Advanced Research Projects Agency (DARPA) for supplying the high-speed cameras used in this study. Insect flight experiments are planned in collaboration with the Department of Zoology, Oxford University.

References

1. K. B. Atkinson, ed., *Close Range Photogrammetry and Machine Vision* (Whittles, 1996).
2. L. Zeng, H. Matsumoto, S. Sunada, and K. Kawachi, "High-resolution method for measuring the torsional deformation of a dragonfly wing by combining a displacement probe with an acousto-optic deflector," Opt. Eng. **35,** 507–513 (1996).
3. L. Zeng, H. Matsumoto, and K. Kawachi, "A fringe shadow method for measuring flapping angle and torsional angle of a dragonfly wing," Meas. Sci. Technol. **7,** 776–781 (1996).
4. L. Zeng, H. Matsumoto, and K. Kawachi, "Divergent-ray projection method for measuring the flapping angle, lag angle and torsional angle of a bumblebee wing," Opt. Eng. **35,** 3135–3139 (1996).
5. A. P. Wilmot and C. P. Ellington, "Measuring the angle of attack of beating insect wings: robust three-dimensional reconstruction from two-dimensional images," J. Exp. Biol. **200,** 2693–2704 (1997).
6. D. Song, H. Wang, L. Zeng, and C. Yin, "Measuring the camber deformation of a dragonfly wing using projected comb fringe," Rev. Sci. Instrum. **72,** 2450–2454 (2001).
7. H. Wang, L. Zeng, and C. Yin, "Measuring the body position, attitude and wing deformation of a free-flight dragonfly by combining a comb fringe pattern with sign points on the wing," Meas. Sci. Technol. **13,** 903–908 (2002).
8. S. Sunada, D. Song, X. Meng, H. Wang, L. Zeng, and K. Kawachi, "Optical measurement of the deformation, motion and generated force of the wings of a moth, *Mythima separata* (Walker)," JSME Int. J., Ser. B **45,** 836–842 (2002).
9. R. I. Hartley, "Euclidean reconstruction from uncalibrated views," in *Proceedings of the DARPA-ESPRIT workshop on Applications of Invariants in Computer Vision* (Springer-Verlag, 1993), pp. 187–202.
10. A. Watt and M. Watt, *Advanced Animation and Rendering Techniques Theory and Practice* (ACM, 1992).
11. D. C. Brown, "Close range camera calibration," Photogramm. Eng. **37,** 855–866 (1971).
12. B. Triggs, P. McLauchlan, R. Hartley, and A. Fiztgibbon, "Bundle adjustment—a modern synthesis," in *Vision Algorithms: Theory and Practice,* Vol. 1883 of Lecture Notes in Computer Science, B. Triggs, A. Zisserman, and R. Szeliski, eds. (Springer, 2000), pp. 298–372.
13. B. Girod, G. Greiner, and H. Niemann, eds., *Principles of 3D Image Analysis and Synthesis* (Kluwer Academic, 2000).
14. N. J. Lawson and J. Wu, "Three-dimensional particle image velocimetry: error analysis of stereoscopic techniques," Meas. Sci. Technol. **8,** 894–900 (1997).